Termination of Indian Ocean Dipole Events in a Coupled General Circulation Model

SURYACHANDRA A. RAO, SEBASTIEN MASSON, JING-JIA LUO, AND SWADHIN K. BEHERA

Frontier Research Center for Global Change/JAMSTEC, Yokohama, Japan

TOSHIO YAMAGATA

Frontier Research Center for Global Change/JAMSTEC, Yokohama, and Department of Earth and Planetary Science, Graduate School of Science, University of Tokyo, Tokyo, Japan

ABSTRACT

Using 200 yr of coupled general circulation model (CGCM) results, causes for the termination of Indian Ocean dipole (IOD) events are investigated. The CGCM used here is the Scale Interaction Experiment-Frontier Research Center for Global Change (SINTEX-F1) model, which consists of a version of the European Community–Hamburg (ECHAM4.6) atmospheric model and a version of the Ocean Parallelise (OPA8.2) ocean general circulation model. This model reproduces reasonably well the present-day climatology and interannual signals of the Indian and Pacific Oceans. The main characteristics of the intraseasonal disturbances (ISDs)/oscillations are also fairly well captured by this model. However, the eastward propagation of ISDs in the model is relatively fast in the Indian Ocean and stationary in the Pacific compared to observations.

A sudden reversal of equatorial zonal winds is observed, as a result of significant intraseasonal disturbances in the equatorial Indian Ocean in November–December of IOD events, which evolve independently of ENSO. A majority of these IOD events (15 out of 18) are terminated mainly because of the 20–40-day ISD activity in the equatorial zonal winds. Ocean heat budget analysis in the upper 50 m clearly shows that the initial warming after the peak of the IOD phenomenon is triggered by increased solar radiation owing to clear-sky conditions in the eastern Indian Ocean. Subsequently, the equatorial jets excited by the ISD deepen the thermocline in the southeastern equatorial Indian Ocean. This deepening of the thermocline inhibits the vertical entrainment of cool waters and therefore the IOD is terminated. IOD events that co-occur with ENSO are terminated owing to anomalous incoming solar radiation as a result of prevailing cloud-free skies. Further warming occurs seasonally through the vertical convergence of heat due to a monsoonal wind reversal along Sumatra–Java. On occasion, strong ISD activities in July–August terminated short-lived IOD events by triggering downwelling intraseasonal equatorial Kelvin waves.

1. Introduction

The Indian Ocean dipole (IOD), a coupled ocean–atmosphere phenomenon in the tropical Indian Ocean (Saji et al. 1999; Webster et al. 1999; Rao et al. 2002), has significant impacts on the surrounding, as well as far-reaching, climate (Behera et al. 1999; Ashok et al. 2001; Guan and Yamagata. 2003; Zubair et al. 2003; Saji and Yamagata 2003; Rao and Behera 2005). During a positive (negative) IOD year, the southeastern Indian Ocean is anomalously cool (warm) and the western Indian Ocean is anomalously warm (cool). In this study, particular attention is paid on positive IOD events. We refer to these events simply as IOD events. The coupled nature of this phenomenon is well documented in the literature (see Yamagata et al. 2004 and references therein).

Several coupled general circulation models (CGCM) have been successful in simulating this phenomenon (Iizuka et al. 2000; Gualdi et al. 2003; Lau and Nath 2004; Yu and Lau 2004; Yamagata et al. 2004). All of these studies showed the capability of CGCMs in simulating the basic characteristics of the IOD and in capturing the processes that are important for the evolution of these events. Ashok et al. (2004) and Tozuka et al. (2007) used CGCM results to study the decadal characteristics of the IOD phenomenon. Behera et al.

Corresponding author address: Suryachandra A. Rao, Frontier Research Center for Global Change/JAMSTEC, 3173-25 Showa-machi, Kanazawa-ku, Yokohama 236-0001, Kanagawa, Japan. E-mail: scrao@jamstec.go.jp

(2005), in addition to showing the capability of CGCMs in simulating the basic characteristics of the IOD, also showed the influence of the model IOD on east African short rains. Some attempts have also been made recently to pursue the prospects of forecasting climate variability over the tropical Indian Ocean sector, specifically extreme positive events of the IOD (Luo et al. 2005a; Wajsowicz 2005). Though many CGCMs are used to understand and forecast IOD phenomena, none of these CGCMs addressed the role of intraseasonal disturbances (ISDs) on the IOD with the lone exception of Gualdi et al. (2003). Using the Scale Interactions Experiment (SINTEX) CGCM, Gualdi et al. (2003) suggested that a particular IOD event in the model does not reach peak strength owing to the presence of strong ISD activity in the Indian Ocean. No further attempts were made to understand the interactions between the ISD and IOD in other coupled models.

Based on composite analysis of major IOD events, Saji et al. (1999) suggests that the IOD is initiated in May–June, peaks in September–October, and decays by December. Many of the CGCMS are successful in simulating this seasonal cycle in composite IOD events (Iizuka et al. 2000; Gualdi et al. 2003; Yamagata et al. 2004; Wajsowicz 2005). Several theories have been put forward to explain the initiation of IOD events (e.g., Annamalai et al. 2003; Kajikawa et al. 2003; P. A. Francis et al. 2005, personal communication). However, few studies have attempted to understand the termination of IOD events. Because of their vast impact on climates of surrounding and far-reaching areas, it is very useful to know how and when IOD events terminate.

Though composite IOD events terminate by December, many of the individual IOD events do not follow this evolution cycle exactly (Rao and Yamagata 2004). This irregular nature of IOD termination was investigated by Rao and Yamagata (2004). They suggested a close relation between the interannual variability in ISD activity and the termination of pure and aborted IOD events. Further, they postulated that the ISD activity in equatorial zonal winds excites equatorial downwelling Kelvin waves and deepens the thermocline in the eastern Indian Ocean, and that it is the major contributor to the termination of IOD events. The role of incoming solar radiation in the termination of IOD events is also suggested by Rao and Yamagata (2004). Owing to a lack of observations, however, they were unable to provide a detailed analysis of the processes involved in the termination of IOD events.

In this study using 200-yr simulation results from a coupled general circulation model we analyze the processes relevant for the termination of IOD events. Particular attention is paid to finding the relationship between the interannual variability of ISD activity in equatorial zonal winds and the termination of IOD events. The roles of seasonal cycles and other processes involved in the termination of IOD events are also investigated. Section 2 provides the details of the coupled model and analysis methods employed in this study. Results from the CGCM relevant to model capability in simulating intraseasonal disturbances and the termination of IOD events are presented in section 3. Section 4 discusses and summarizes the results of the present study.

2. Model and data analysis methods

The CGCM used here is SINTEX-F1 [SINTEX-Frontier Research Center for Global Change (FRCGC) model, version 1.0], a modified version of a CGCM developed under the framework of the European Union's Scale Interaction Experiment project. The model is based on versions of the European Community–Hamburg (ECHAM4.6) and the Ocean Parallelise (OPA8.2) ocean model coupled together and developed to run on the Earth Simulator. The atmosphere component of the CGCM, T106L19 ECHAM4.6 (Roeckner et al. 1996), is coupled to the ocean component of the OPA8.2 through the Ocean Atmosphere Sea Ice Soil (OASIS 2.4; Valcke et al. 2000) coupling software package. The OPA8.2 ocean modeling system was developed by the Laboratoire d'Oceanographie Dynamique et de Climatologie (LODYC) team in Paris (Madec et al. 1998). It is a finite-difference ocean general circulation model and solves the primitive equations with nonlinear equations of state on an Arakawa C grid. The model domain extends from 78°S to 90°N. The model uses a tripolar grid with latitude–longitude resolution of $2.0° \times 2.0°$ cosine (latitude) with increased meridional resolution of up to 0.5° near the equator. There are 31 levels in the vertical with 14 levels in the upper 150 m. Vertical eddy diffusivity and viscosity coefficients are computed from a 1.5 turbulent closure scheme. No flux adjustment is employed in SINTEX-F1. Gualdi et al. (2003) described the original SINTEX model. Details of the modified version of this model (i.e., SINTEX-F1) are provided in many recent studies (Luo et al. 2003; Masson et al. 2005; Luo et al. 2005b). The 5-day-mean output, after removing the linear trend, from the last 200 yr of the total 220 yr of model integration is used for the analysis. To study the intraseasonal disturbances, we have applied a Laczos bandpass filter with 100 weights and half-power frequency cutoffs of 20 and 100 day^{-1} to the precipitation and wind datasets. The statistical significance of the results presented in this study is determined by a Student's two-tailed t test, unless otherwise specified.
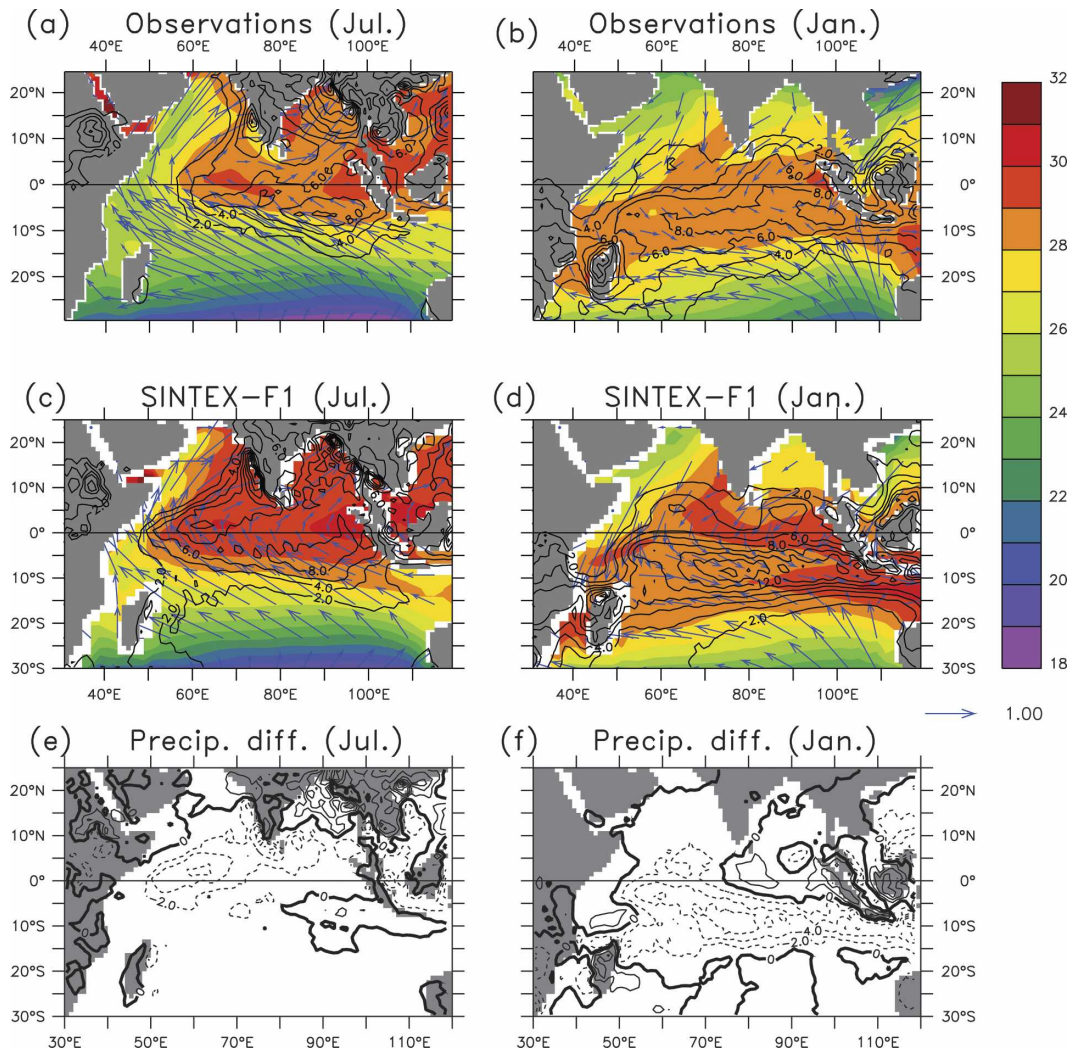
FIG. 1. Mean climatological SST (shaded), winds stress (vectors), and precipitation (contours) in July and January from the (a),(b) observations and (c),(d) model. Units: SST, °C; wind stress, dyn cm^{-2}; and precipitation, mm day^{-1}. Observational SST is taken from Reynolds et al. (2002), wind stress is from the ECMWF reanalysis, and precipitation is from GPCP 1° daily data. Reference wind stress vector is shown at bottom of (d). Precipitation differences between the observed and the model in (e) July and (f) January.

3. Results

a. Model mean climatology and intraseasonal disturbances

The ability of the model to reproduce the observed mean climatology and basic characteristics of the ISD is evident in Figs. 1–3. The mean climate parameters (SST, wind stress, and precipitation) in July and January, from both the model and observations, are shown in Fig. 1. The January and July climate parameters are selected to represent the summer and winter monsoon conditions, respectively. Model SSTs are relatively warm by 1°C, both in July and in January, as compared to the observations derived from Reynolds et al. (2002).

The surface wind stress in the model is relatively weak (strong) in July (January) compared to the European Centre for Medium-Range Weather Forecasts (ECMWF) reanalysis data. The model simulated a weak atmospheric Somali jet (Findlater jet) compared to the reanalysis data. Therefore, the upwelling along the coasts of Africa and Arabia is also weak and SSTs in those regions are relatively warm compared to the observations. The model precipitation distribution, in general, agrees very well with the observations both in July and in January. A relatively large precipitation total (2–4 mm day^{-1}) is observed in the western equatorial Indian Ocean and along the west coast of India in the model in July (Fig. 1e) as a result of warmer model
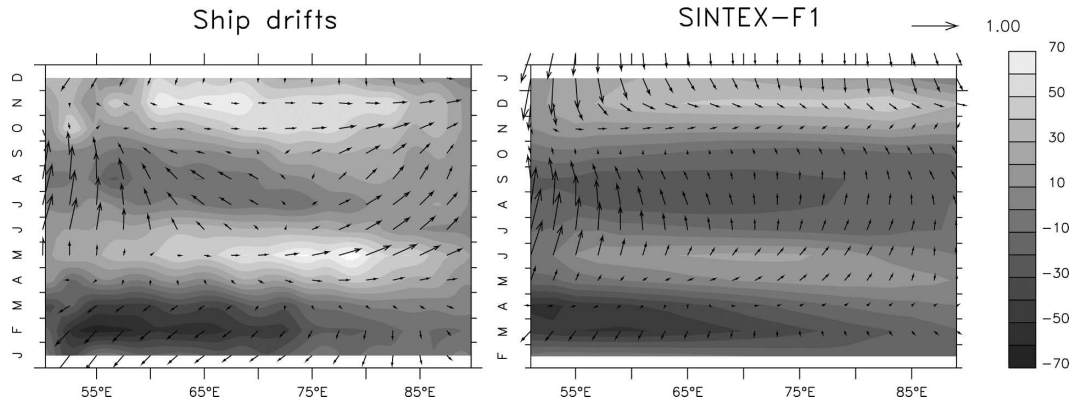
FIG. 2. Equatorial surface zonal currents derived from (a) ship drifts and (b) the model. Equatorial wind stress vectors averaged in the region between 2°N and 2°S are also overlaid. Units of currents are cm s^{-1}.

SSTs in those places. In January, the model produces higher precipitation south of the equator (2–6 mm day^{-1}). The interannual and intraseasonal variances, in these relatively higher precipitation zones in the model, also show strong variances as compared to the observations (not shown). For further information on this model bias, refer to Luo et al. (2005b). On the whole,

the spatial distribution of the climatological parameters is reasonably well reproduced by the model and to some extent the magnitude of these variables is also reproduced.

Oceanic features of the model, particularly surface equatorial currents (Yoshida/Wyrtki jets), are also compared with the observations. The ocean zonal cur-
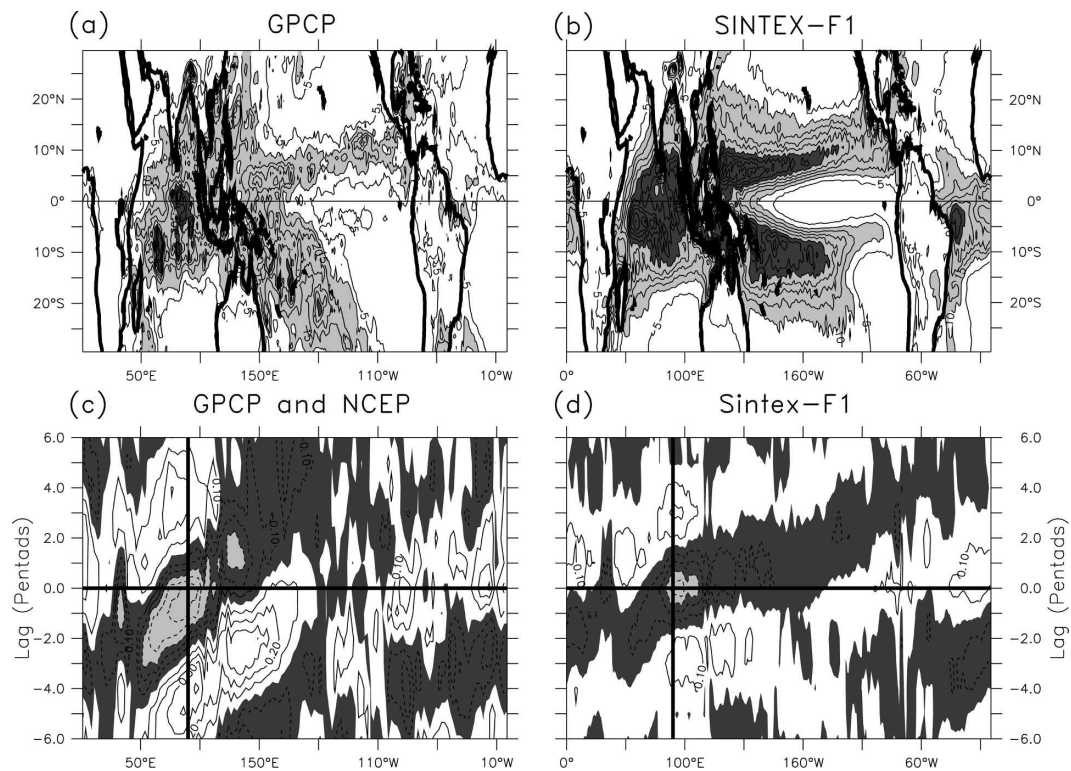

FIG. 3. Variance of 20–100-day bandpass-filtered precipitation for the October–April period from (a) GPCP and (b) the SINTEX-F1 model. Contour interval is 5 (mm day^{-1})$^{-2}$. Lag correlation plots of precipitation averaged between 10°N and 10°S with 200-hPa velocity potential at 90°E also averaged between 10°N and 10°S from (c) observations [GPCP (precipitation)/NCEP (velocity potential)] and (d) SINTEX-F1.

rents in the model at 5 m along with ship drift observations from Rao et al. (1989) are shown in Fig. 2. In general, the model climatological jets appear to be weaker compared to the observations. This pattern is even more evident in spring. This is in response to weak equatorial winds in the model climatology during spring. Furthermore, this patterns is also a result of the strong interannual and intraseasonal variabilities of the equatorial jets in the model. Similarly, the strong interannual and intraseasonal variabilities in equatorial jets are also evident in the observations (Han et al. 1999; Schott and McCreary 2001; Masumoto et al. 2005). At times the model jets are stronger than the observed jets (see section 4) in the 200-yr simulation.

Th variances of 20–100-day bandpass-filtered precipitation anomalies for the months between October and April are shown in Fig. 3. The model shows strong variance in precipitation as compared to the observations. This difference is particularly strong in the western tropical Pacific owing to the model bias in the western Pacific warm pool region (Luo et al. 2005b). The warm pool SST in the western South Pacific stretches zonally to the east, approximately to 120°W, and the equatorial cold tongue of SST extends too far west in this CGCM. These model SST errors introduce a double ITCZ in the western tropical Pacific and a dry region in the western equatorial Pacific (Luo et al. 2005b). As a result, the variance of the precipitation in the western equatorial (southern tropical) Pacific is lower (higher) compared to the observations. However, the spatial pattern of the variance is similar to the observed patterns, except in the South Pacific convergence zone. This bias is common in many coupled models (Latif et al. 2001). In fact, many of the CGCMs even fail to capture a reasonable spatial distribution of the ISD (cf. Gualdi et al. 1999; Innes et al. 2003).

The eastward propagation of 20–100-day oscillations in the model is examined in the following. For this purpose, the precipitation anomalies averaged between 10°S and 10°N are correlated with the velocity potential anomalies at 200 hPa averaged between the same latitudinal belts at 90°E. This shows how the surface anomalies propagate with respect to the large-scale upper-atmospheric circulation. Beginning at lag −4 to lead 4 pentads, the observations clearly show the eastward propagation of these correlation patterns from the western Indian Ocean to the date line (Fig. 3c). It may also be observed that the correlation coefficients are very strong even at 6 pentads lead. However, these eastward propagations are restricted to the Indian Ocean in the model (Fig. 3d). In the western Pacific the correlation patterns do not propagate, which is probably a result of the dry bias in the model. This station-

ary bias of the ISD in the western Pacific is also common in many CGCMs without flux corrections (cf. Gualdi et al. 1999; Innes et al. 2003). The model ISD propagates (correlation coefficients) from the western Indian Ocean to the eastern Indian Ocean within about 30 days. This propagation is relatively fast compared to the observed ISD propagation (Fig. 3c). Furthermore, the correlation coefficients in the analysis of the model results are found to be weaker. One possibility for weaker correlation is the longer data period in the analysis of the model results as compared to that in the observations. Slight increases in the correlation coefficients are observed, when we considered shorter time periods for the analysis. The above analysis revealed that the variance of the ISD in the model is stronger than the observed variance and its eastward propagation is limited to the Indian Ocean in the CGCM. Since the present study relies on the ISD in the Indian Ocean, we believe that the model biases in the western Pacific do not influence our conclusions drawn using this CGCM. Furthermore, the results presented in this study agree reasonably well with those of the observations shown in Rao and Yamagata (2004).

The interannual variability of the model IOD events is also very well captured by the SINTEX-F1 CGCM (see Yamagata et al. 2004; Behera et al. 2005; Tozuka et al. 2007). The model reproduces the reversal in sign of the SST anomalies (SSTA) across the equatorial basin with the easterly wind stress along the equator during IOD events. However, the model SSTA in the eastern Indian Ocean during IOD events extends far to the west (Behera et al. 2005). This bias is also common in other CGCMs (cf. Iizuka et al. 2000; Gualdi et al. 2003). It may be noted here that this bias is similar to the ENSO bias in almost all CGCMs (Latif et al. 2001), where the eastern equatorial Pacific warming extends too far to the west. The model IOD statistics are also reasonably well reproduced in this CGCM, with the dipole SSTA appearing as the second EOF mode, explaining 23% of the interannual SSTA variance, and the relation between the IOD and ENSO is also comparable with observations (Yamagata et al. 2004; Behera et al. 2005; Tozuka et al. 2007).

b. Termination of IOD events

Rao and Yamagata (2004) suggested that the pure and aborted IOD events in the most recent four decades terminate in response to ISD activity in the equatorial zonal winds. On the other hand, IOD events that co-occur with El Niño events terminate due to changes in incoming solar radiation and the seasonal reversal of monsoon winds. Following Rao and Yamagata (2004), we have categorized IOD events into three main cat-

TABLE 1. Causes for termination of model IOD events.

Cause of termination	Pure IOD years	IOD years that co-occur with El Niño	Aborted IOD events
In response to ISD in equatorial zonal winds	0027, 0029, 0031, 0041, 0046, 0051, 0059, 0070, 0074, 0081, 0086, 0098, 0111, 0141, 0184	0158, 0178, 0187	0069, 0028, 0080, 0108, 0172
In response to seasonal deepening of thermocline and heating due to incoming solar radiation	0062, 0099, 0188	0023, 0036, 0040, 0044, 0054, 0077, 0085, 0091, 0092, 0094, 0103, 0124, 0151, 0161, 0192, 0210, 0217	

egories depending on their association with ENSO and their longevity: (I) strong IOD [dipole mode index exceeds 1 standard deviation (std dev)] events that occur without concurrent El Niños in the tropical Pacific (referred to as pure IOD events), (II) strong IOD events that co-occur with El Niños (Niño-3 index exceeds 0.5 std dev), and (III) aborted IOD events that were terminated before reaching the peak strength. The total numbers of strong IOD events in SINTEX-F1 for categories I, II, and III are 18, 20, and 5, respectively (Table 1).

The SSTAs averaged in the southeastern equatorial

Indian Ocean (10°S–equator and 90°–110°E) for the six strongest IOD events in categories I and II and the four strongest IOD events in category III are shown in Fig. 4. The SSTAs for pure IOD events (i.e., category I) start evolving during June (gradual decrease of SSTA), reach peak strength by October–November, and decay by the end of November–December. IOD events in category II start evolving during July and reach their peak strength by October–November; however, they terminate by the end of December. Category III events, on the other hand, terminate by August. For the purposes of comparison, the observed SSTAs in the south-
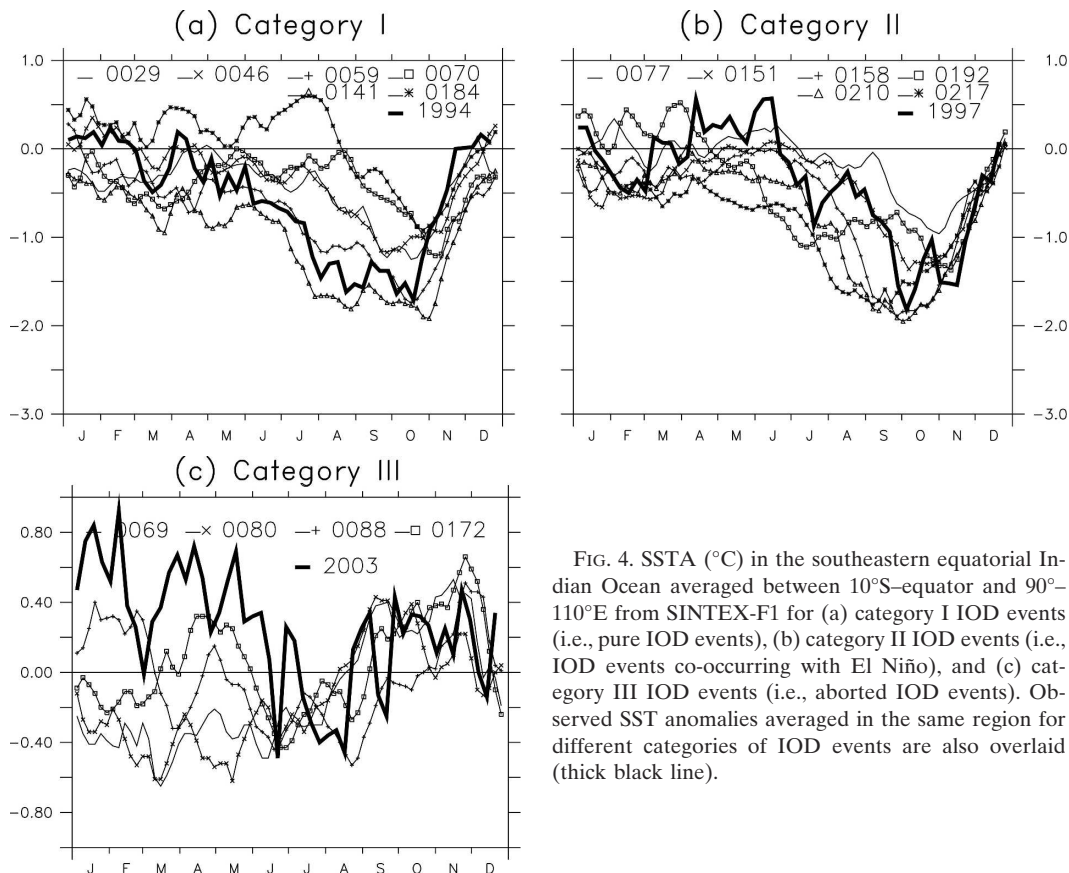

FIG. 4. SSTA (°C) in the southeastern equatorial Indian Ocean averaged between 10°S–equator and 90°–110°E from SINTEX-F1 for (a) category I IOD events (i.e., pure IOD events), (b) category II IOD events (i.e., IOD events co-occurring with El Niño), and (c) category III IOD events (i.e., aborted IOD events). Observed SST anomalies averaged in the same region for different categories of IOD events are also overlaid (thick black line).
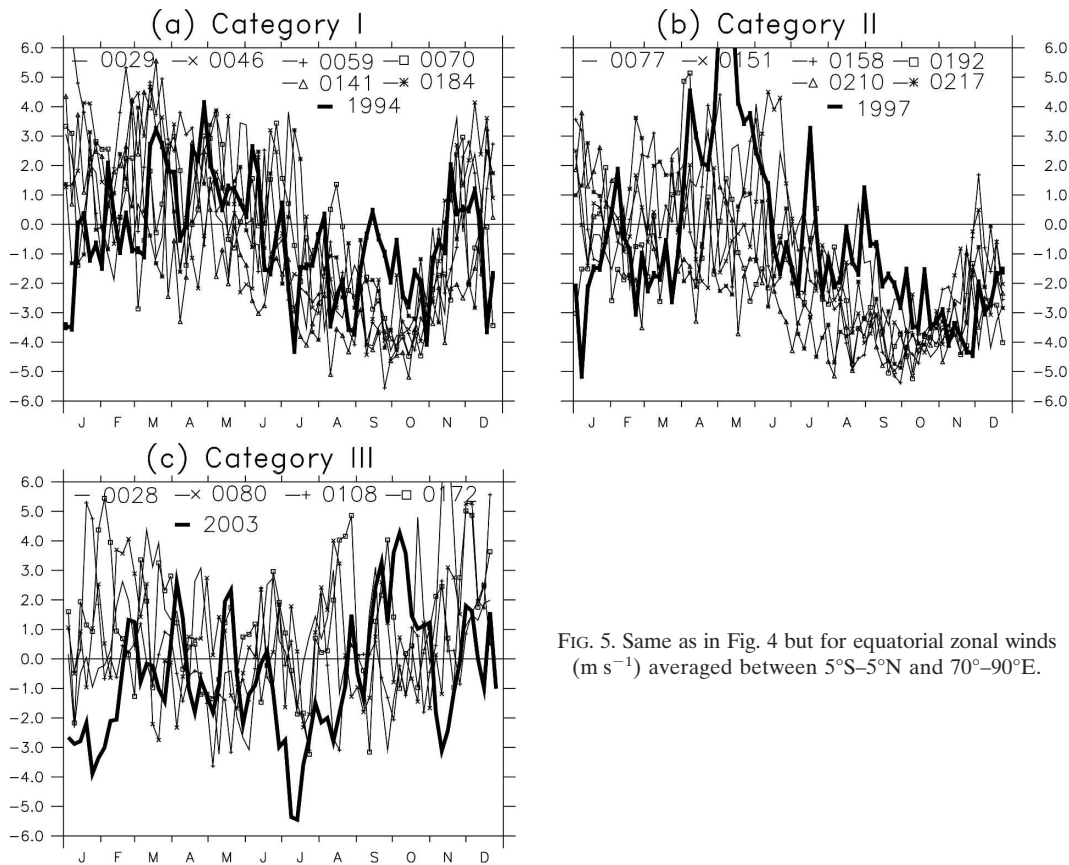
FIG. 5. Same as in Fig. 4 but for equatorial zonal winds (m s^{-1}) averaged between 5°S–5°N and 70°–90°E.

eastern equatorial Indian Ocean for categories I, II, and III IOD events are also shown (in bold black line) in Fig. 4. Model IOD events evolve similarly to the observed IOD events [bold black lines in Figs. 4a–c; also see Rao and Yamagata (2004)]. Pure IOD events such as the 1967 and 1994 events terminate well before December, while IOD events that co-occurred with strong El Niño events such as 1997 terminate by December. Furthermore, aborted IOD events such as 1979 and 2003 terminate by August (Rao and Yamagata 2004). The close resemblance between the observed and model SSTAs further demonstrates the capability of the model to reproduce the observed interannual variability.

Equatorial zonal winds averaged between 5°S–5°N and 70°–90°E for all three categories of IOD events are shown in Fig. 5. A sudden reversal of equatorial zonal winds in November is observed prior to the termination of category I events. No such sudden reversal in equatorial zonal winds is observed for category II events, with the lone exception being the model IOD event in 0158 yr. Nonetheless, relaxation of the easterly winds is observed prior to the termination of the majority of these events. On the other hand, strong intraseasonal

disturbances in equatorial zonal winds with strong westerlies in August are observed for short-lived category III events. The model equatorial zonal winds compare reasonably well with the observations (bold black lines in Fig. 5).

To understand the termination of the model IOD events, a heat budget analysis in the upper 50 m is carried out in the southeastern equatorial Indian Ocean. To show the capability of the model in reproducing the observed heat budget processes, the composite IOD heat budget is shown in Fig. 6. All category I and II IOD events (38 events) are composed together by considering the model calendar. The corresponding heat budget terms are presented in Fig. 6. In general, the initial cooling tendency (black curve in Fig. 6) in the southeastern equatorial Indian Ocean is dominantly forced by the latent heat loss (not shown) in response to strong southeasterlies along the coast of Sumatra and Java. Similar results were also obtained in previous studies (e.g., Vinayachandran et al. 2002; Li et al. 2002) using OGCMs forced with observed winds and heat fluxes. After the initiation of the IOD event (after June), the cooling tendency closely follows the horizontal and vertical divergences of the heat transport in the
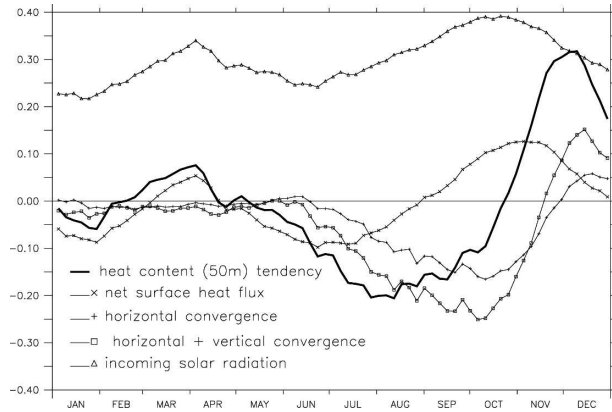
FIG. 6. Composite heat budget terms for the southeastern equatorial Indian Ocean for all IOD events (categories I and II). Contribution of incoming solar radiation is also shown (＿＿Δ). Units are in °C (5 day)$^{-1}$.

model. The vertical divergence is due to the cold water that is upwelled into the mixed layer in response to local southeasterlies and also due to remote easterlies along the equator that drive anomalous upwelling Kelvin waves. The horizontal divergence is a result of the westward transport of cool surface waters. Similar results, using OGCMs, have been reported previously by some studies (e.g., Murtugudde et al. 2000; Vinayachandran et al. 2002; Li et al. 2002).

Since the evolution cycles of IOD events differ from event to event (Figs. 4 and 5), we prefer to study the thermodynamic processes separately for the six strongest IOD events in categories I and II and for the four events in category III. Heat budget terms, for all of the three above categories, are shown in Figs. 7a–c. The heat budget terms for October–December are discussed for category I and II events and June–August months are considered for category III events in order to highlight the termination processes.

When the cooling tendency (solid line in Fig. 7a) reaches its peak in the category I events, the net surface heat flux gradually increases in response to increased incoming solar radiation. This is due to cloud-free conditions in the southeastern equatorial Indian Ocean. This increase in incoming solar radiation is the main contributor to the initial warming tendency of the model heat content in October. Oceanic processes (horizontal and vertical convergence) of the heat transport also play an equally important role for this initial warming after the relaxation of the equatorial zonal winds (shown as vertical lines in Figs. 7a and 7b). However, the warming tendency after the initial warming is maintained mainly by the vertical and horizontal convergence of the heat transport for pure IOD events. We

notice that the major contribution for the horizontal convergence of heat comes from the zonal advection of heat (Fig. 7a). The dominant contribution of the vertical and horizontal convergence of the heat transport over the net surface flux (gray shading in Fig. 7a) for the model temperature tendency clearly highlights the importance of the ocean dynamics for the termination of category I IOD events. Similar tendency terms for the 1994 observed IOD event are also reported by Vinayachandran et al. (2002).

A heat budget analysis for category II IOD events is shown in Fig. 7b. Similar to the category I events, the cooling tendency for category II events is also maintained primarily through the horizontal and vertical divergence of the heat transport. However, marked differences are observed during and after the initial warming tendency. The warming tendency of the model heat content, beyond the initial warming, is maintained by incoming solar radiation until late November. However, the vertical and horizontal convergences of the heat transports play important roles just prior to the termination of category II IOD events. Nevertheless, the contribution of the oceanic processes is relatively low compared to those for category I events, with the lone exception being the model IOD event in 0158 yr (cf. gray shadings in Figs. 7a and 7b).

On the other hand, the termination of category III IOD events is mainly in response to the vertical and horizontal convergence of the heat transport, since the tendency of the net surface heat flux during this period supports surface cooling.

c. Intraseasonal disturbances and termination of IOD events

It is clear from Figs. 4 and 7a that the sudden reversal of the equatorial zonal winds caused the early termination of category I IOD events through the dominant oceanic processes (horizontal and vertical convergence of the heat transport). It is of interest to find out what caused these sudden changes in the equatorial zonal winds. For this purpose, 20–100-day bandpass-filtered precipitation anomalies are composed by considering all of the category I IOD events. The composites are made in such a way that the second pentad of each event coincided with the time when the strength of the equatorial zonal wind stress, averaged between 5°S–5°N and 70–90°E, diminished to −0.05 dyn cm^{-2}. Clear eastward propagation of bandpass-filtered positive precipitation anomalies can be seen for category I IOD events in Fig. 8a. The precipitation anomalies propagate from the western Indian Ocean to the eastern Indian Ocean in 20–30 days. Along the path of these
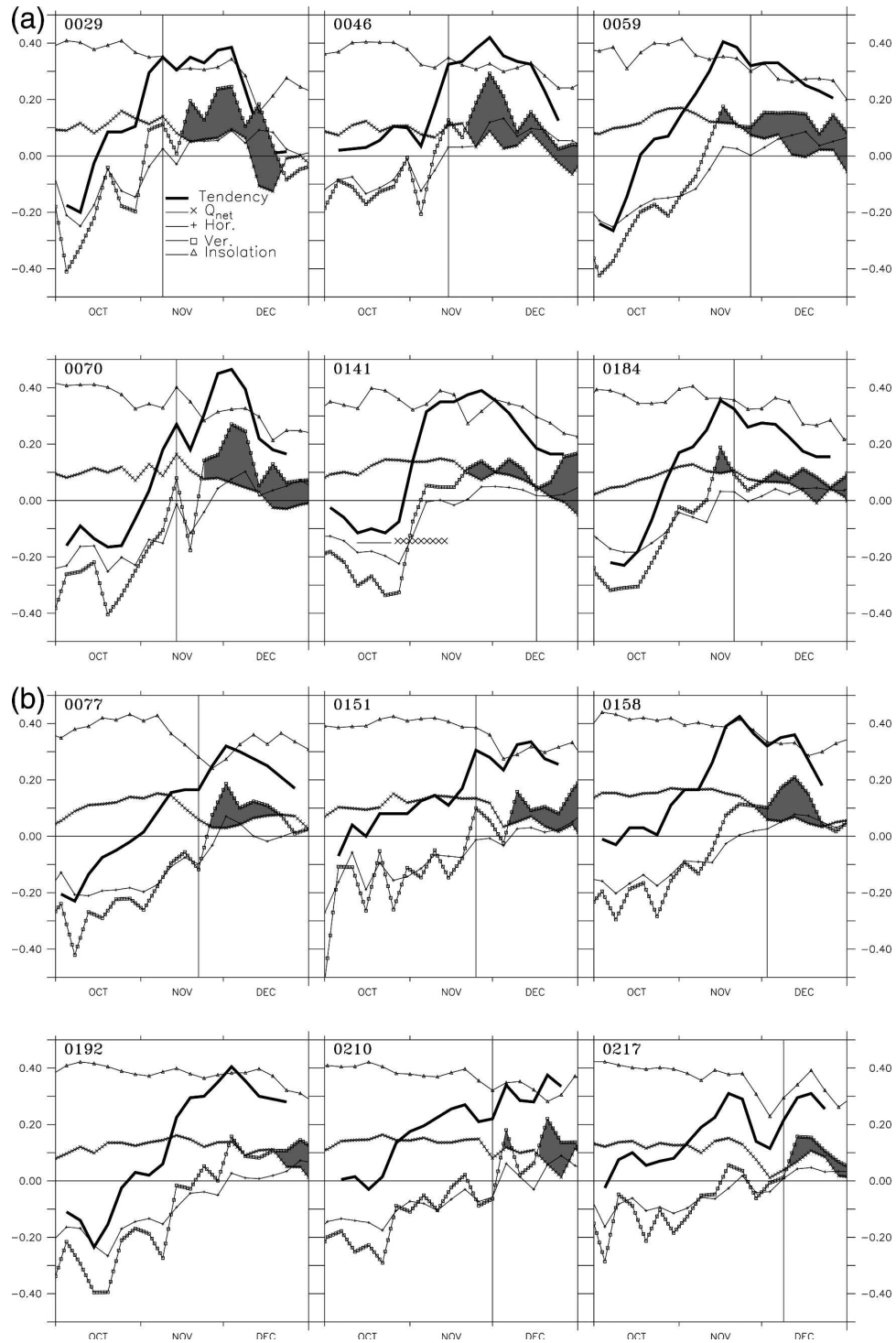
FIG. 7. Same as in Fig. 6 but for the strongest IOD events in (a) category I, (b) category II, and (c) category III. Vertical lines represent the time coinciding with the relaxation of the equatorial zonal wind stress (-0.05 dyn cm^{-2}). Numerals at top left within each plot are model years. The regions where oceanic processes (horizontal and vertical convergence of heat transport) dominate the net surface heat fluxes are shaded in gray.
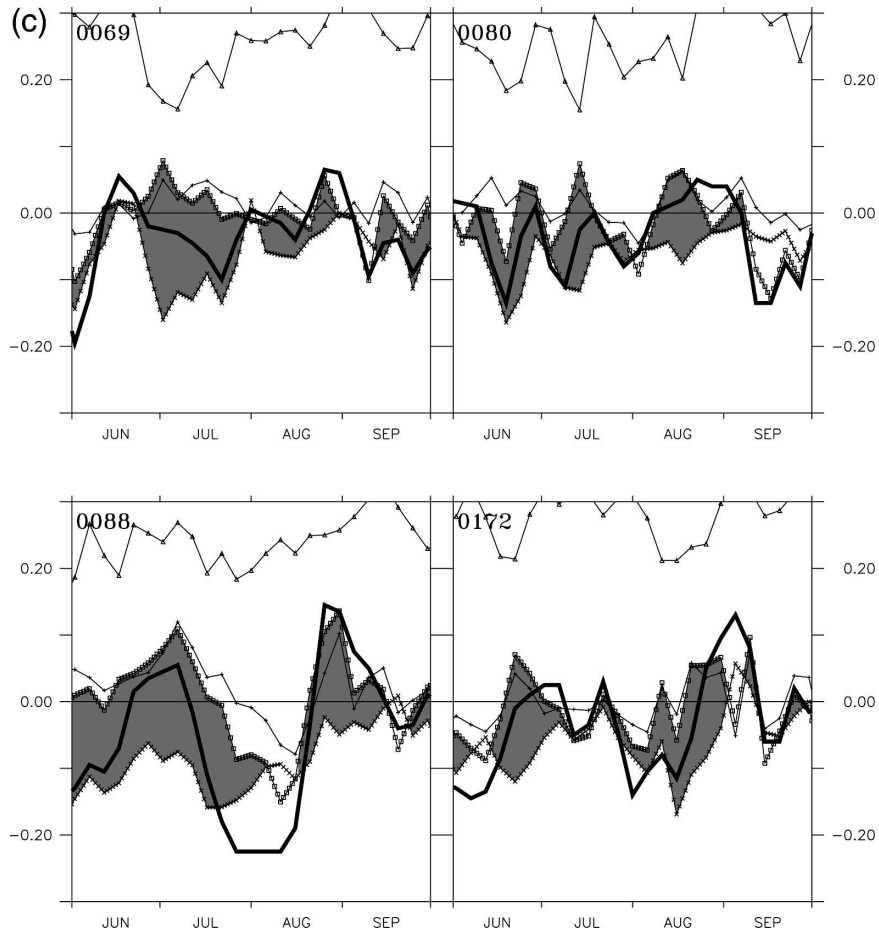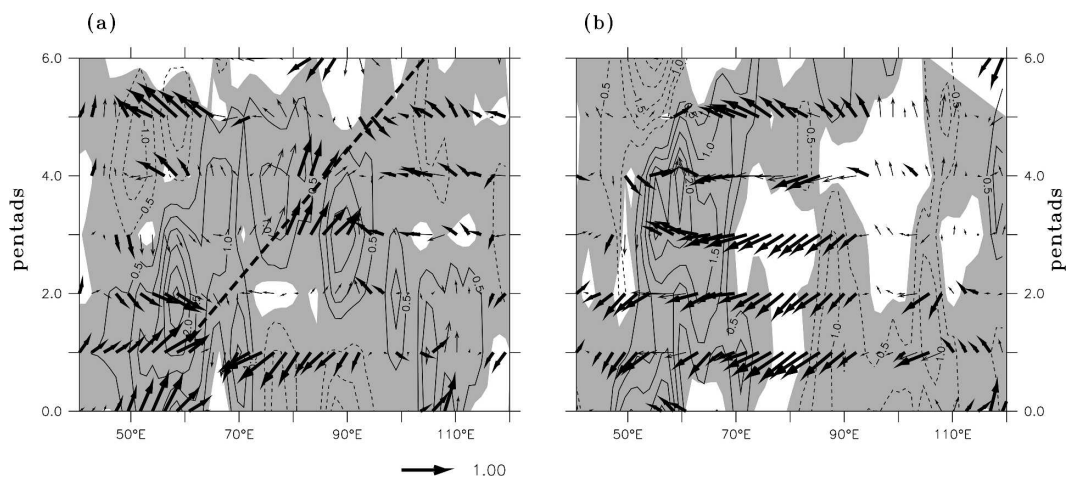
FIG. 7. (*Continued*)

FIG. 8. Composite 20–100-day bandpass-filtered precipitation anomalies averaged between 10°S and 10°N (contours in mm day^{-1}) for (a) category I and (b) category II events. Second pentad in each composite coincides with the time when the equatorial zonal wind stress relaxed to −0.05 dyn cm^{-2}. Wind vectors (in m s^{-1}) are also overlaid. Precipitation (wind) anomalies above the 95% confidence limit are shaded (bold arrows). Reference wind vector is shown at bottom. Dashed line in (a) shows the eastward propagation of the precipitation anomalies.

precipitation anomalies the strengthened westerly anomalies are also observed. These westerly wind anomalies drive anomalous downwelling oceanic Kelvin waves along the equator. Model wind stress anomalies together with model currents at 5 m, at pentad intervals and bandpass filtered between 20 and 100 days, are shown in Fig. 9, for a particular IOD event in model year 0029. Figure 9 clearly shows the anomalous eastward currents particularly in the central and eastern equatorial Indian Ocean, which reaches the eastern Indian Ocean by late November 0029. This downwelling Kelvin wave deepens the thermocline in the southeastern Indian Ocean and enhances the vertical convergence of the heat transport, thereby terminating the IOD event.

The manifestation of this ISD signal in the equatorial zonal winds is also witnessed from the wavelet spectrum analysis. At 20–40 days a conspicuous signal prior to termination, in November–December of category I IOD events, is clearly seen in Fig. 10a. However, between the initiation and termination phases of many of the IOD events, no significant 20–40-day signal is observed. This finding is once again in agreement with the observational evidence shown in Rao and Yamagata (2004). The major difference between the observations and the model results, however, is that the signal is at a 30–60-day period in the observations. This is because of the model ISD bias as discussed in section 3a. As in the observations, these 20–40-day intraseasonal disturbances drive equatorial westerlies as shown in Figs. 8 and 9.

The following sequence of events clearly demonstrates the link among these various processes: 1) initial warming tendency (Fig. 7a) in early October–November due to incoming solar radiation, 2) relaxation of equatorial zonal winds in mid-November (Fig. 5; timing of the relaxation of the easterly wind anomalies shown as a vertical line in Figs. 7a and 7b), 3) 20–40-day oscillations in equatorial zonal winds (Fig. 10a), 4) excitation of a downwelling Kelvin wave (Fig. 9) in response to strong westerly equatorial winds, and 5) vertical and horizontal convergence of the heat transport in response to all of the above processes. Most of the pure IOD events (15 out of 18; about 83%) terminate in this sequence. However, a few (3 out of 18, i.e., 16%) events terminate mainly by increased incoming solar radiation as a result of cloud-free conditions in the eastern Indian Ocean followed by seasonal deepening of the thermocline in the east (not shown).

The wavelet spectrum for category III IOD events is shown in Fig. 7c. It is clearly evident from Fig. 7c that category III events could not develop into strong events because of the strong ISD activity in summer. Strong
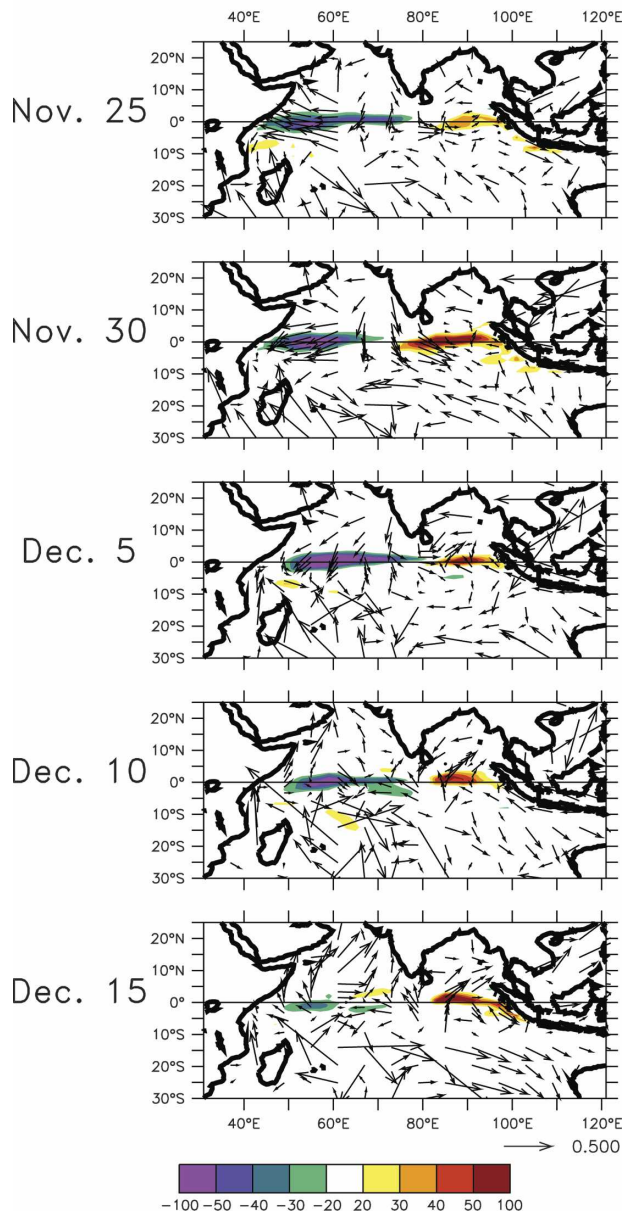

FIG. 9. The 20–100-day bandpass-filtered surface wind stress anomalies (vectors) and anomalies of the surface (5 m) zonal currents (shading) from SINTEX-F1 for the model IOD event in year 0029. Reference wind stress vector is shown at bottom.

20–40-day oscillations are seen in the summer of these IOD events. The heat budget analysis clearly shows that the termination is caused mainly by the deepening of the thermocline and the resultant vertical convergence of heat into the mixed layer (Fig. 7c). The strong ISD activity in the model generated frequent equatorial jets, in addition to the known seasonal equatorial jets
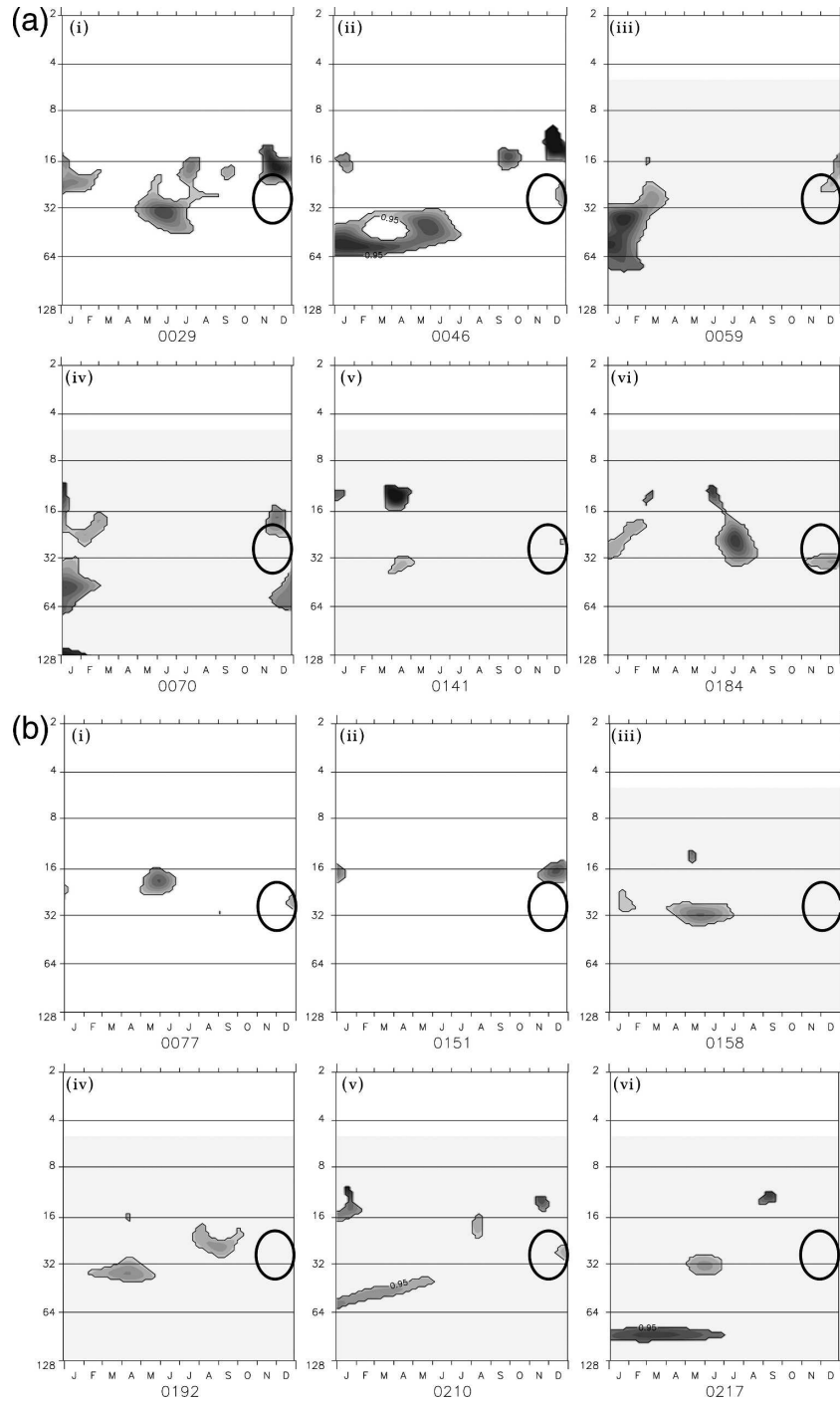
FIG. 10. (a) Wavelet spectrum of equatorial zonal winds averaged between 5°S–5°N and 70°–90°E for different years in (a) category I, (b) category II, and (c) category III IOD events. Wavelet spectrum is normalized with the global wavelet spectrum and only values above the 95% confidence limit are shown. Ellipses in these diagrams show time around the IOD termination for a 20–40-day period. Units along the ordinate are period in days.
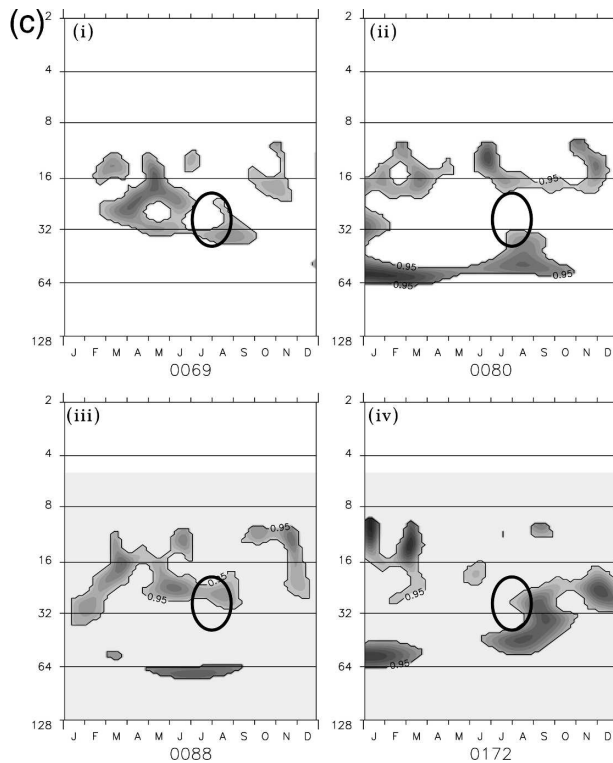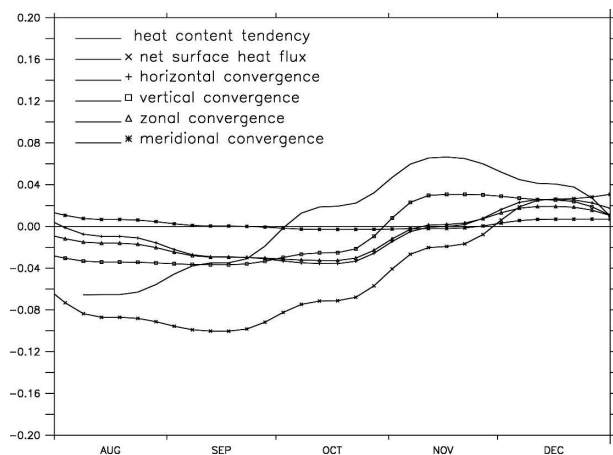
FIG. 10. (*Continued*)

FIG. 11. Seasonal mean heat budget terms in the southeastern Indian Ocean from August to December. Units in $°C (5 \text{ day})^{-1}$.

during aborted IOD events (Fig. 14c). Equatorial jets on intraseasonal time scales in the eastern equatorial Indian Ocean were recently observed by Masumoto et al. (2005) and various mechanisms for the generation of these intraseasonal jets, using an ocean model, have been proposed by Han (2005).

d. Seasonal cycle and termination of IOD events

Composite 20–100-day bandpass-filtered precipitation anomalies for category II events are shown in Fig. 8b. In contrast to the composite for the category I events, the composite for the category II events does not show any significant eastward propagation of the precipitation anomalies. Similarly, the equatorial winds do not reverse as in Fig. 5 for category I events. The intraseasonal wavelet spectrum of category II IOD events for equatorial zonal winds (Fig. 10b) further confirms this fact. Prior to the termination of IOD events, no significant 20–40-day oscillations are observed in the equatorial zonal winds, with the lone exception being the model IOD event in year 0158. Since very few category II events are associated with ISD activity prior to termination (Table 1), the composite of the precipitation anomalies (Fig. 8b) does not show eastward propagation. Some activity at the peripherals

of the 20–40-day band (shown as red eclipse) is observed for model years 0077, 0151, and 0158. In this study we prefer not to pay attention to these subseasonal oscillations.

As mentioned in section 3b the initial warming tendency, for category II events, is primarily maintained by heating in response to incoming solar radiation until the end of November. The seasonal heat budget terms for the southeastern equatorial Indian Ocean are shown in Fig. 11. The warming tendency of the seasonal mean temperature in the southeastern equatorial Indian Ocean is maintained by the net surface heat flux and the convergence of the zonal and vertical heat transports in response to seasonal eastward jets (Fig. 2). However, the contribution of this mean seasonal convergence of heat for thetemperature tendency is relatively small compared to its contribution during anomalous events (Fig. 7).

Even though the equatorial zonal winds do not reverse after November, the horizontal and vertical convergence of the heat transport is taking place for category II events; it is interesting to find out the reasons for this change in heat transport. Composites of anomalous winds, for both categories (I and II events) along the Sumatra–Java coasts are shown in Fig. 12. The timing of these composites coincides with the second pentad after the relaxation of the equatorial zonal winds. Interestingly, we do not find any significant change in the winds along the Sumatra–Java coasts in the category I IOD composite. However, in the category II composite, we find a complete reversal of the winds (from southeasterlies to northwesterlies) along these coasts, in response to the seasonal monsoon reversal. These local winds inhibit the local upwelling and there-
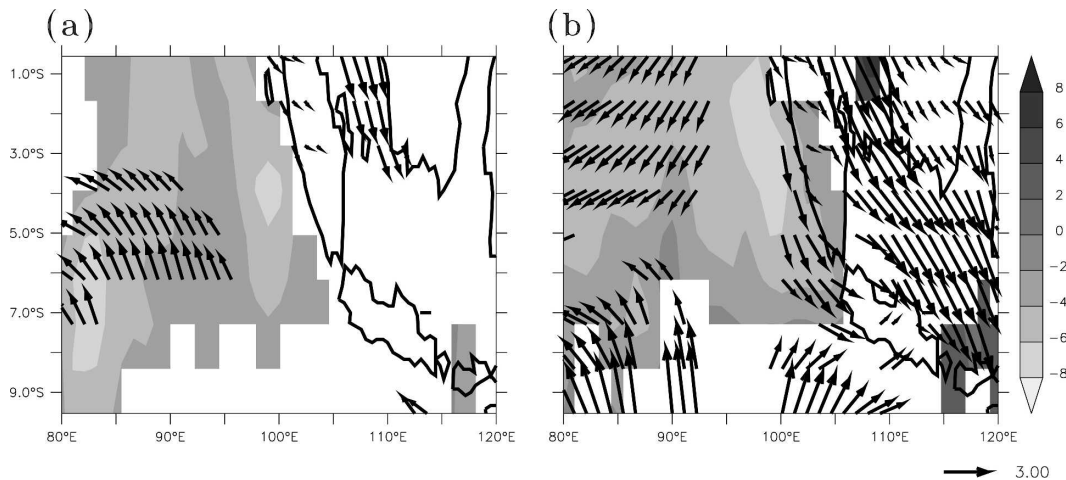
FIG. 12. Composite wind (vectors, m s^{-1}) and precipitation anomalies (mm day^{-1}) after two pentads of relaxation of equatorial zonal wind stress for (a) category I and (b) category II IOD events.

fore result in the horizontal and vertical convergence of the heat transport into the southeastern equatorial Indian Ocean. Most of the category II IOD events (17 out of 20; 85%) terminate due to this seasonal deepening of the thermocline and increase in the incoming solar radiation. The remaining few events (Table 1) terminate in a manner similar to that of the category I events, in response to ISD activity in the equatorial zonal winds.

On the other hand, since category I events terminate earlier than category II events, before the monsoon reversal along the Sumatra–Java coasts, we do not find significant changes in winds along these coasts. This once again confirms the role of the equatorial zonal winds in bringing the horizontal and vertical convergence of the heat transport into the southeastern equatorial Indian Ocean during category I events.

4. Summary and discussion

In this study, the processes involved in the termination of IOD events are investigated using the SINTEX-F1 CGCM. The model reproduces the observed interannual and intraseasonal signals reasonably well in the tropical Indian Ocean. This is one of the motivations for using this CGCM to understand the termination processes involved in IOD events. However, as with any other CGCM, the present CGCM also suffers from a few model biases. These biases are evident particularly in the western tropical Indian Ocean and the western tropical Pacific. Because of weaker simulated monsoon winds in the western Indian Ocean, the model SST is warmer as compared to the observations, particularly during the summer monsoon. In the western Pacific, the

ISD characteristics are not well reproduced by this CGCM, because of a strong warm bias in the southwestern Pacific and a cold bias in the western equatorial Pacific.

In the present study, IOD events are categorized into three different groups based on their association with El Niño and their longevity. It is shown here that pure IOD events (category I) terminate primarily in response to ISD activity in the equatorial zonal winds. ISD activity at 20–40 days is observed in the model, as opposed to 30–60-day oscillations in the observations, prior to the termination of pure IOD events. Model ISD activity excites downwelling Kelvin waves/eastward jets and deepens the thermocline in the southeastern equatorial Indian Ocean. This results in the vertical convergence of the heat transport into the mixed layer and therefore it accelerates the termination of IOD events. However, not all model pure IOD events terminate in response to ISD activity. About 83% of the model pure IOD events terminate because of ISD activity in equatorial zonal winds. The remaining model IOD events in this category terminate in response to seasonal warming. This warming results from increased incoming solar radiation due to cloud-free conditions and the seasonal thermocline deepening brought about by eastward equatorial jets and the seasonal reversal of monsoon winds.

Though the role of the ISD in the termination of category I IOD events is emphasized, the role of the seasonal cycle cannot be ignored completely. This is due to the seasonal phase locking of the equatorial zonal winds. In boreal spring and boreal fall (i.e., transition periods between winter and summer mon-
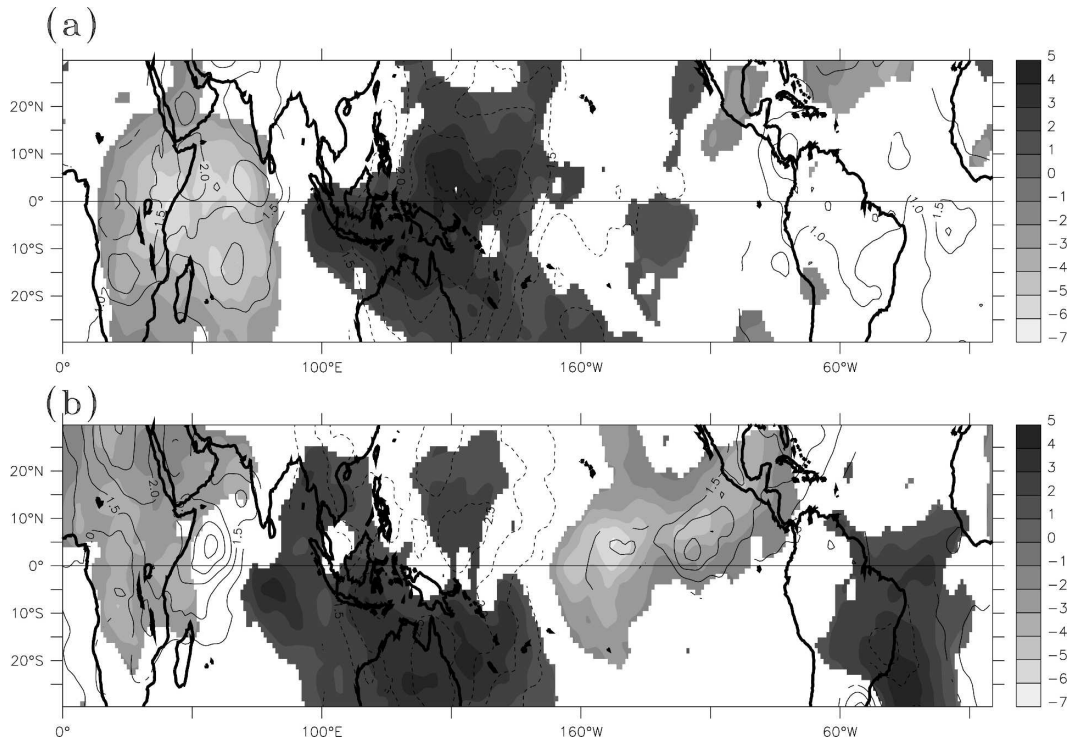
FIG. 13. Composite velocity potential at 200 (shaded) and 850 hPa (contours) prior to the termination of IOD events. Units are in 10^{-6} m^2 s^{-1}. Only values above the 95% confidence limit are shown.

soons) strong westerly winds occur along the equator (Vinayachandran et al. 1999; Schott and McCreary 2001, and references therein). The strength of these winds are either enhanced or reduced depending on the anomalous conditions in the Indian Ocean during IOD events. For example, ISD activity in the equatorial Indian Ocean enhanced the fall westerly winds during category I events (Fig. 5). On the other hand, strong El Niño conditions in the tropical Pacific might reduce the strength of these westerly winds in fall (see discussion below).

Some of the category II events that co-occur with El Niño also terminate due to ISD activity in equatorial zonal winds; however, the percentage of these events is very small (15%). The majority of the category II events (85%) terminate because of increased incoming solar radiation and seasonal deepening of the thermocline. It is found that during the majority of the El Niño events that co-occurred with IOD events the strength of ISD is insignificant prior to the termination of IOD events. On the other hand, strong ISD activity in summer inhibited further development of category III IOD events. This anomalously strong ISD activity generates intraseasonal jets in the equatorial Indian Ocean (Fig. 14c) and inhibits further development of category III IOD events.

It is interesting to investigate the cause of the continuance of equatorial easterly wind anomalies during category II IOD events in November–December. One immediate suggestion is the absence of ISD activity. Another possibility could be an active El Niño in the tropical Pacific. In general, when IOD events are active in the tropical Indian Ocean, we observe a single anomalous Walker cell within the Indian Ocean with a descending limb over Indonesia and an ascending limb over the western Indian Ocean (Yamagata et al. 2004; Fig. 13a). However, when IOD events co-occur with El Niño, we observe two anomalous Walker cells in the Tropics (Yamagata et al. 2004; Fig. 13b). An active Walker cell in the tropical Pacific can drive easterly wind anomalies in the equatorial Indian Ocean. Hence, we do not observe a reversal of the equatorial zonal winds during the majority of the category II IOD events. However, a monsoon reversal along the Sumatra–Java coast (Fig. 12) can stop the local upwelling and therefore the category II IOD events may terminate.

In addition to playing a role in terminating IOD events, the absence of ISD activity in equatorial zonal winds prior to IOD events plays an important role in the initiation of these events. For example, during model category I IOD years 0059, 0070, and 0141, no
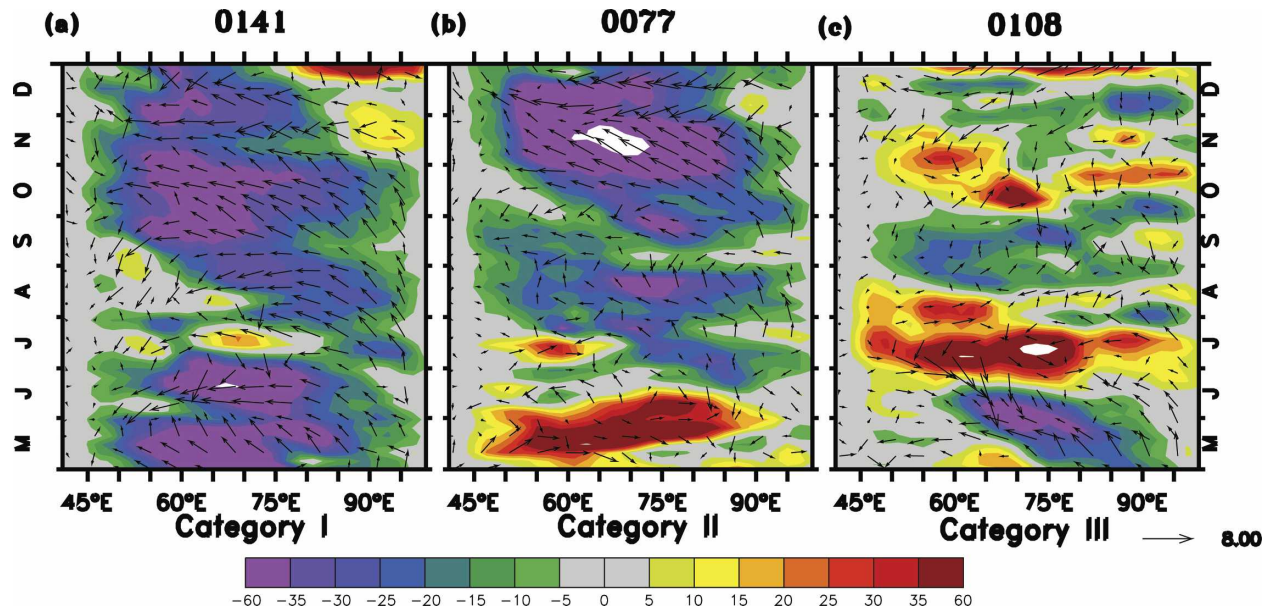
FIG. 14. Model equatorial zonal currents anomalies (cm s^{-1}) in the top layer (5 m) for various model IOD years. Model year is shown at top of each plot. Anomalies of the equatorial winds (m s^{-1}) averaged between 2°S and 2°N are overlaid.

significant ISD activity with 20–40-day oscillations is observed in May–June (Fig. 10a). As a result, the model spring jets are weaker as compared to spring jets in other IOD years (Fig. 14a); therefore, the initiation of the IOD (gradual drop of SST in the southeastern equatorial Indian Ocean) can take place earlier (Fig. 4a) than that of other IOD years with significant ISD activity in May–June (e.g., years 0029 and 0184). These conditions are similar to the observed 1994 IOD event. In 1994, the spring jet was reportedly weak (Vinayachandran et al. 1999). On the other hand, for the majority of the category II IOD events, significant ISD activity is observed in May–June (Fig. 10b), and the initiation of the model IOD events generally starts after July. Such conditions are also observed in the real world for category II IOD events (e.g., the 1997 event; Fig. 4b).

Though we find significant ISD activity in equatorial zonal winds prior to the termination of the majority of the pure IOD events, the cause of their sudden appearance is not yet understood. One probable scenario is that a slight weakening of IOD events (warming of the southeastern equatorial Indian Ocean), initially, in response to incoming solar radiation can enhance the possibility of the presence of ISD activity (particularly in the absence of another major interannual signal; El Niño). Since the southeastern equatorial Indian Ocean lies in a warm pool region, small changes in the SST

anomaly here can induce large atmospheric responses. Therefore, it is possible that a slight weakening of cool SST anomalies in this region can enhance the probability of the initiation of ISD activity. Another possibility is the excessive heating of the western equatorial Indian Ocean during an IOD event. Carefully designed CGCM–AGCM experiments are needed for detailed investigation of these issues. Further, the reason for the absence of significant ISD activity prior to the initiation of category I IOD events also needs to be explored.

REFERENCES

Annamalai, H., R. Murtugudde, J. Potemra, S. P. Xie, P. Liu, and B. Wang, 2003: Coupled dynamics over the Indian Ocean: Spring initiation of the zonal mode. *Deep-Sea Res.,* **50,** 2305–2330.

Ashok, K., Z. Guan, and T. Yamagata, 2001: Impact of the Indian Ocean dipole on the decadal relationship between the Indian monsoon rainfall and ENSO. *Geophys. Res. Lett.,* **28,** 4499–4502.

——, W. Chan, T. Motoi, and T. Yamagata, 2004: Decadal variability of the Indian Ocean dipole. *Geophys. Res. Lett.,* **31,** L24207, doi:10.1029/2004GL021345.

Behera, S. K., R. Krishnan, and T. Yamagata, 1999: Unusual ocean–atmosphere conditions in the tropical Indian Ocean during 1994. *Geophys. Res. Lett.,* **26,** 3001–3004.

——, J.-J. Luo, S. Masson, T. Yamagata, P. Delecluse, S. Gualdi, and A. Navarra, 2005: Paramount impact of the Indian Ocean dipole on the east African short rains: A CGCM study. *J. Climate,* **18,** 4514–4530.

Gualdi, S., A. Navarra, and M. Fischer, 1999: The interannual variability in the tropical Indian Ocean as simulated by a CGCM. *Geophys. Res. Lett.,* **26,** 2973–2976.

——, E. Guilyardi, A. Navarra, S. Masina, and P. Delecluse, 2003: The interannual variability in the tropical Indian Ocean as simulated by a CGCM. *Climate Dyn.,* **20,** 567–582.

Guan, Z., and T. Yamagata, 2003: The unusual summer of 1994 in East Asia: IOD teleconnections. *Geophys. Res. Lett.,* **30,** 1544, doi:10.1029/2002GL016831.

Han, W., 2005: Origins and dynamics of the 90-day and 30–60-day variations in the equatorial Indian Ocean. *J. Phys. Oceanogr.,* **35,** 708–728.

——, J. P. McCreary, D. L. T. Anderson, and A. J. Mariano, 1999: On the dynamics of the eastward surface jets in the equatorial Indian Ocean. *J. Phys. Oceanogr.,* **29,** 2191–2209.

Iizuka, S., T. Matsuura, and T. Yamagata, 2000: The Indian Ocean SST dipole simulated in a coupled general circulation model. *Geophys. Res. Lett.,* **27,** 3369–3372.

Inness, P. M., J. M. Slingo, E. Guilyardi, and J. Cole, 2003: Simulation of the Madden–Julian oscillations in a coupled general circulation model. Part II: The role of the basic state. *J. Climate,* **16,** 365–382.

Kajikawa, Y., T. Yasunari, and R. Kawamura, 2003: The role of local Hadley circulation over the western Pacific on the zonally asymmetric anomalies over the Indian Ocean. *J. Meteor. Soc. Japan,* **81,** 259–276.

Latif, M., and Coauthors, 2001: ENSIP: The El Niño Simulation Intercomparison Project. *Climate Dyn.,* **18,** 255–276.

Lau, N.-C., and M. J. Nath, 2004: Coupled GCM simulation of atmosphere–ocean variability associated with zonally asymmetric SST changes in the tropical Indian Ocean. *J. Climate,* **17,** 245–265.

Li, T., Y. Zhang, E. Lu, and D. Wang, 2002: Relative role of dynamic and thermodynamic processes in the development of the Indian Ocean dipole: An OGCM diagnosis. *Geophys. Res. Lett.,* **29,** 2110, doi:10.1029/2002GL015789.

Luo, J. J., S. Masson, S. Behera, P. Delecluse, S. Gualdi, A. Navarra, and T. Yamagata, 2003: South Pacific origin of the decadal ENSO-like variations as simulated by a coupled GCM. *Geophys. Res. Lett.,* **30,** 2250, doi:10.1029/2003GL018649.

——, ——, ——, S. Shingu, and T. Yamagata, 2005a: Seasonal climate predictability in a coupled OAGCM using a different approach for ensemble forecast. *J. Climate,* **18,** 4474–4497.

——, ——, E. Roeckner, G. Madec, and T. Yamagata, 2005b: Reducing climatology bias in an ocean–atmosphere CGCM with improved coupling physics. *J. Climate,* **18,** 2344–2360.

Madec, G., P. Delecluse, M. Imbard, and C. Levy, 1998: OPA

version 8.1 ocean general circulation model reference manual. LODYC/IPSL Tech. Note 11, LODYC/IPSL, Paris, France, 91 pp.

Masson, S., and Coauthors, 2005: Impact of barrier layer on winter–spring variability of the southeastern Arabian Sea. *Geophys. Res. Lett.,* **32,** L07703, doi:10.1029/2004GL021980.

Masumoto, Y., H. Hase, Y. Kuroda, H. Matsuura, and K. Takeuchi, 2005: Intraseasonal variability in the upper layer currents observed in the eastern equatorial Indian Ocean. *Geophys. Res. Lett.,* **32,** L02607, doi:10.1029/2004GL021896.

Murtugudde, R. G., J. P. McCreary, and A. J. Busalacchi, 2000: Oceanic processes associated with anomalous events in the Indian Ocean with relevance to 1997–1998. *J. Geophys. Res.,* **105,** 3295–3306.

Rao, R. R., R. L. Molinari, and J. F. Festa, 1989: Evolution of the climatological near-surface thermal structure of the tropical Indian Ocean, I. Description of mean monthly mixed layer depth, and sea surface temperature, surface current, and surface meteorological fields. *J. Geophys. Res.,* **94,** 10 801–10 815.

Rao, S. A., and T. Yamagata, 2004: Abrupt termination of Indian Ocean dipole events in response to intraseasonal disturbances. *Geophys. Res. Lett.,* **31,** L19306, doi:10.1029/2004GL020842.

——, and S. K. Behera, 2005: Subsurface influence on SST in the tropical Indian Ocean: Structure and interannual variability. *Dyn. Atmos. Oceans,* **39,** 103–135.

——, ——, Y. Masumoto, and T. Yamagata, 2002: Interannual variability in the subsurface tropical Indian Ocean with a special emphasis on the Indian Ocean dipole. *Deep-Sea Res. II,* **49,** 1549–1572.

Reynolds, R. W., N. A. Rayner, T. M. Smith, D. C. Stokes, and W. Wang, 2002: An improved in situ and satellite SST analysis for climate. *J. Climate,* **15,** 1609–1625.

Roeckner, E., and Coauthors, 1996: The atmospheric general circulation model ECHAM4: Model description and simulation of present day climate. Max-Plank-Institut für Meteorologie Rep. 218, Hamburg, Germany, 90 pp.

Saji, N. H., and T. Yamagata, 2003: Possible impacts of Indian Ocean dipole mode events on global climate. *Climate Res.,* **25,** 151–169.

——, B. N. Goswami, P. N. Vinayachandran, and T. Yamagata, 1999: A dipole mode in the tropical Indian Ocean. *Nature,* **401,** 360–363.

Schott, F. A., and J. P. McCreary, 2001: The monsoon circulation of the Indian Ocean. *Prog. Oceanogr.,* **51,** 1–123.

Tozuka, T., J.-J. Luo, S. Masson, and T. Yamagata, 2007: Decadal modulations of the Indian Ocean dipole in the SINTEX-F1 coupled GCM. *J. Climate,* **20,** 2881–2894.

Valcke, S., L. Terray, and A. Piacentini, 2000: The OASIS coupler user guide, version 2.4. Tech. Rep. TR/CMGC/00-10, CERFACS, Toulouse, France, 85 pp.

Vinayachandran, P. N., N. H. Saji, and T. Yamagata, 1999: Response of the equatorial Indian Ocean to an anomalous wind event during 1994. *Geophys. Res. Lett.,* **26,** 1613–1616.

——, S. Iizuka, and T. Yamagata, 2002: Indian Ocean dipole mode events in an ocean general circulation model. *Deep-Sea Res. II,* **49,** 1573–1596.

Wajsowicz, R. C., 2005: Forecasting extreme events in the tropical Indian Ocean sector climate. *Dyn. Atmos. Oceans,* **39,** 137–151.

Webster, P. J., A. Moore, J. Loschnigg, and M. Leban, 1999: Coupled ocean–atmosphere dynamics in the Indian Ocean during 1997–98. *Nature,* **40,** 356–360.

Yamagata, T., S. K. Behera, J.-J. Luo, S. Masson, M. Jury, and S. A. Rao, 2004: Coupled ocean–atmosphere variability in the tropical Indian Ocean. *Earth Climate: The Ocean–Atmosphere Interaction, Geophys. Monogr.,* Vol. 147, Amer. Geophys. Union, 189–212.

Yu, J.-Y., and K. M. Lau, 2004: Contrasting Indian Ocean SST variability with and without ENSO influence: A coupled atmosphere–ocean GCM study. *Meteor. Atmos. Phys.,* **90,** doi:10.1007/s00703-004-0094-7.

Zubair, L., S. A. Rao, and T. Yamagata, 2003: Modulation of Sri Lankan *Maha* rainfall by the Indian Ocean dipole. *Geophys. Res. Lett.,* **30,** 1063, doi:10.1029/2002GL015639.